Electronic supplementary information

Power-free, filter-free and high-performance narrowband ZnO/BaTiO$_3$/GaN heterojunction ultraviolet photodetector induced by synergetic plasmonic and ferroelectric effects

Kai Tang, Shulin Sha, Maosheng Liu, Mengxin Yu, Peng Wan, Caixia Kan, Daning Shi*, Mingming Jiang*

College of Physics, MIIT Key Laboratory of Aerospace Information Materials and Physics, Key Laboratory for Intelligent Nano Materials and Devices, Nanjing University of Aeronautics and Astronautics, Nanjing 211106, China

***Corresponding authors:**

Daning Shi (Email: shi@nuaa.edu.cn);

Mingming Jiang (Email: mmjiang@nuaa.edu.cn).

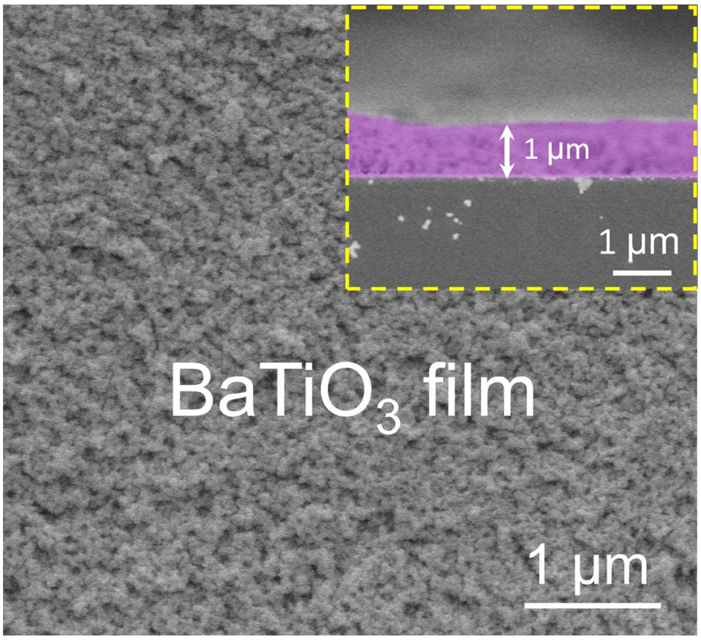

Figure S1. SEM images of the surface and cross-sectional of $BaTiO_3$ nanocrystals film on the p-GaN substrate.

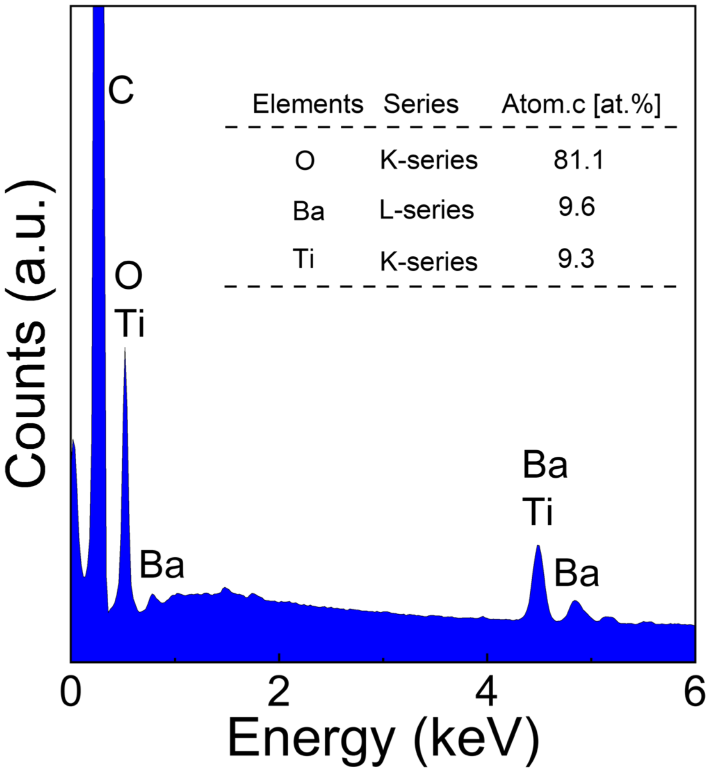

Figure S2. EDX spectra of $BaTiO_3$ nanocrystals film.

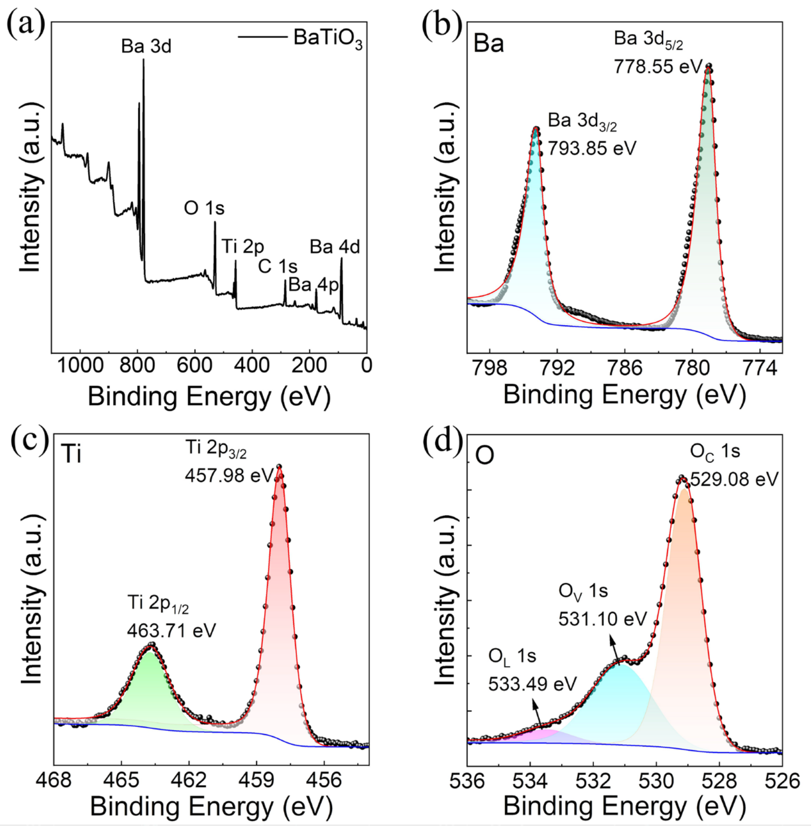

Figure S3. (a) XPS survey spectrum of the BaTiO$_3$ nanocrystals film. High resolution XPS spectra for (b) Ba 3d, (c) Ti 2p and (d) O 1s, respectively.

Fig. S3(a) is the XPS wide-scan spectrum of BaTiO$_3$ film over a range of 0 ~ 1100 eV. Obvious signals corresponding to Ti, Ba, and O further reveal the growth of BTO. Fig. S3(b)-(c) show the XPS fine spectra of Ba, Ti, and O. The Ba 3d spectrum consists of two peaks located at 778.55 (Ba 3d$_{5/2}$) and 793.85 eV (Ba 3d$_{3/2}$) from the Ba^{2+} oxide state. In addition, the Ti 2p spectrum possesses two peaks located at 457.98 and 463.71 eV, corresponding to Ti 2p$_{3/2}$ and Ti 2p$_{1/2}$ of Ti^{4+} in BTO, respectively. No obvious signal for Ti^{3+} can be found in the Ti 2p XPS spectrum. The O 1s spectrum consists of three symmetrical signals, that is, at the binding energies of 529.08 eV, 531.10 eV, and 533.49 eV, which are assigned to the chemisorbed oxygen species (O$_C$), oxygen vacancy (O$_V$), and lattice oxygen (O$_L$), respectively. Fine fitting yields a relative ratio of oxygen vacancies, O$_V$/(O$_L$+O$_V$), equal to 84.5%, which is considered to be controlled by the solution-precursor decomposition cum crystallization process during the BaTiO$_3$ fabrication.[1]

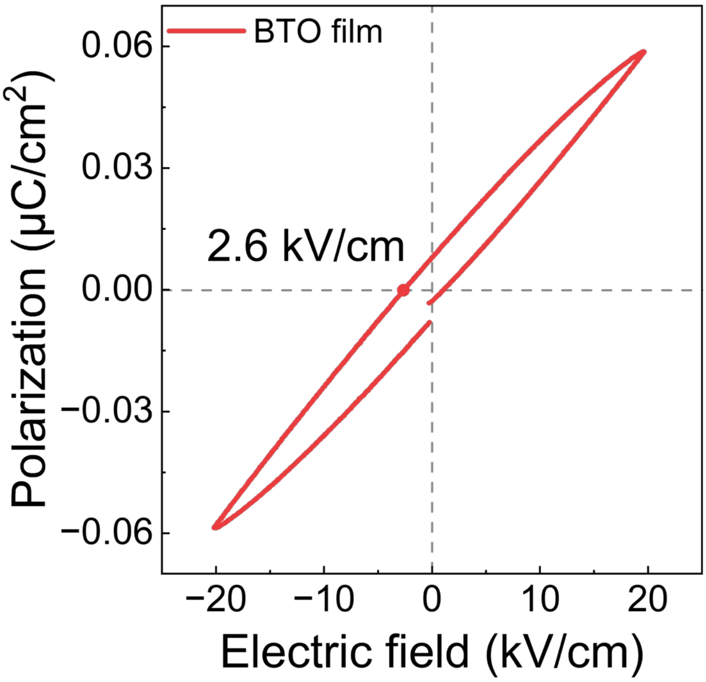

Figure S4. The *P-E* hysteresis loop of $BaTiO_3$ nanocrystals film at room temperature.

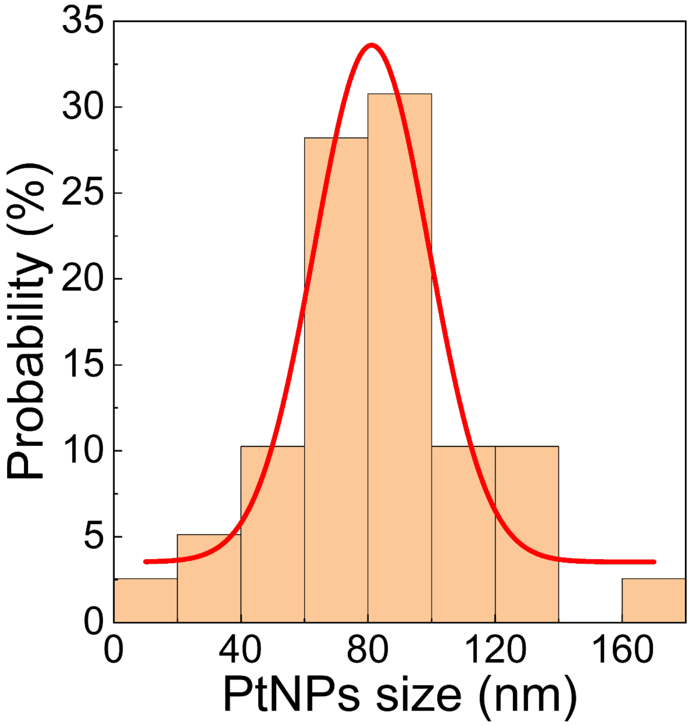

Figure S5. Particle size distribution of PtNPs.

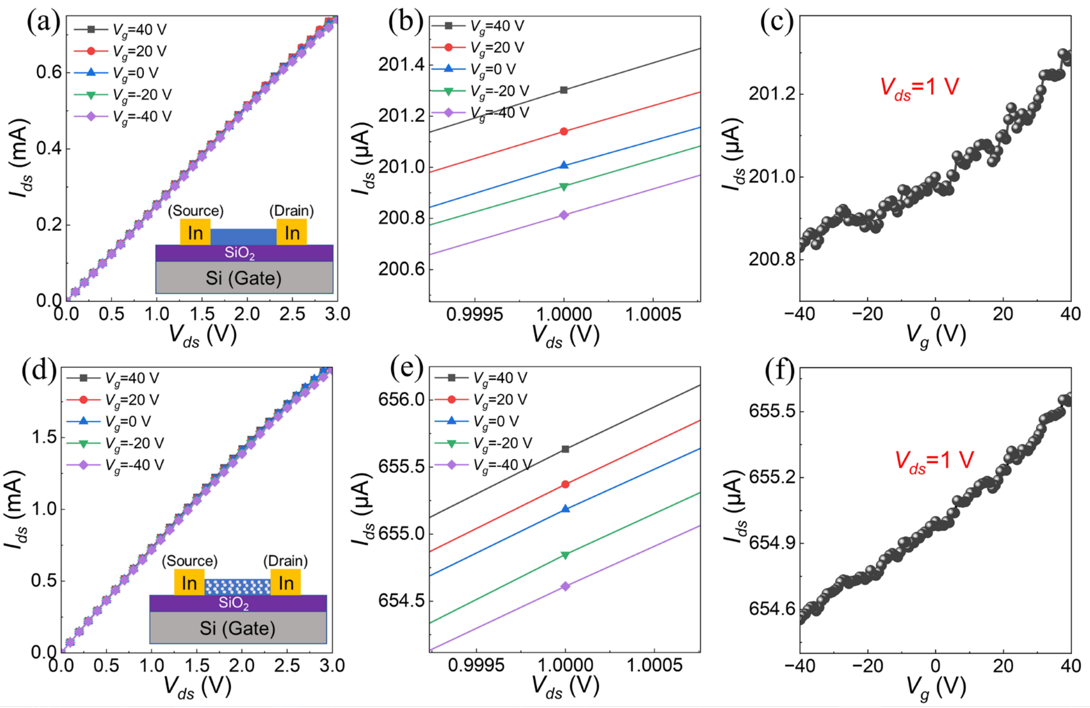

Figure S6. Electrical transport characterization of an individual MW-based FET devices, in which a ZnO:Ga MW was uncoated and coated with PtNPs. (a) I_{ds}-V_{ds} curves of a naked ZnO:Ga MW based FET device at different gate voltage (V_g). Inset: schematic illustration of a ZnO:Ga MW based FET. (b) The partial view of the I_{ds}-V_{ds} curves at around V_{ds} = 1 V. (c) I_{ds}-V_g curve at V_{ds} = 1 V. As the ZnO:Ga MW FET device was surface-coated using PtNPs, (d) V_g-dependent I_{ds}-V_{ds} curves measurement result, and the inset shows a diagram of PtNPs@ZnO:Ga MW based FET. (e) The partial view of the I_{ds}-V_g curves at around V_{ds} = 1 V. (f) I_{ds}-V_g plotted at V_{ds} = 1 V.

The modulation of PtNPs on electrical transport characteristics of a ZnO:GaMW was measured using a single wire-based field-effect transistors (FETs). Two In particles are utilized as the (source/drain) electrode on both ends of a single wire, which is placed on a SiO_2/Si substrate, with Si serving as the gate electrode. A schematic diagram of a ZnO:Ga MW FET device is shown in the inset of Fig. S6(a). The drain-source current versus drain-source voltage (I_{ds}-V_{ds}) curves measured at different gate voltages (V_g) are shown in Fig. S6(a), which reveals that the output characteristics of ZnO:Ga MW FET show a linear behavior. It confirms the Ohmic contacts between the ZnO:Ga MW and In electrodes. Fig. S6(b) shows an amplified I_{ds}-V_{ds} curves near V_{ds} = 1 V. Clearly, the

I_{ds} increases (declines) with the forward (reverse) V_g. In Fig. S6(c), the I_{ds} curve demonstrates a nearly linear behavior with continuous variation in V_g (-40 V to 40 V). There is a strong positive correlation between I_{ds} and V_g, implying that the ZnO:Ga MWs have a n-type semiconductor conductivity characteristic. As the ZnO:Ga MW FET device was surface-modified using PtNPs with desired dimension, electrical measurement was also conducted. The obtained I_{ds}-V_{ds} curves at different V_g are shown in Figs. S6(d) and (e). From the graphs, the PtNPs@ZnO:Ga MW FET has higher Ids than that of the pristine device. While at V_{ds} = 1.0 V, the I_{ds}-V_g plot in the Fig. S6(f) exhibits higher slope, i.e. higher transconductance gain (g_m). The amplification factor of the FET was related by g_m, which is a function of the mobility, channel length, and temperature of the semiconductor material.

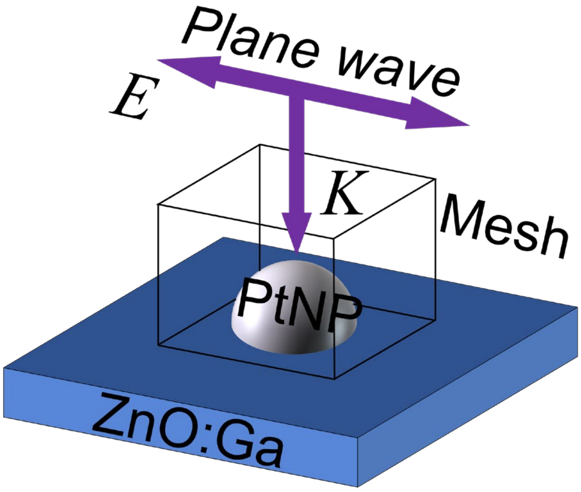

Figure S7. The schematics of PtNP/ZnO:Ga configuration under the plane wave excitation.

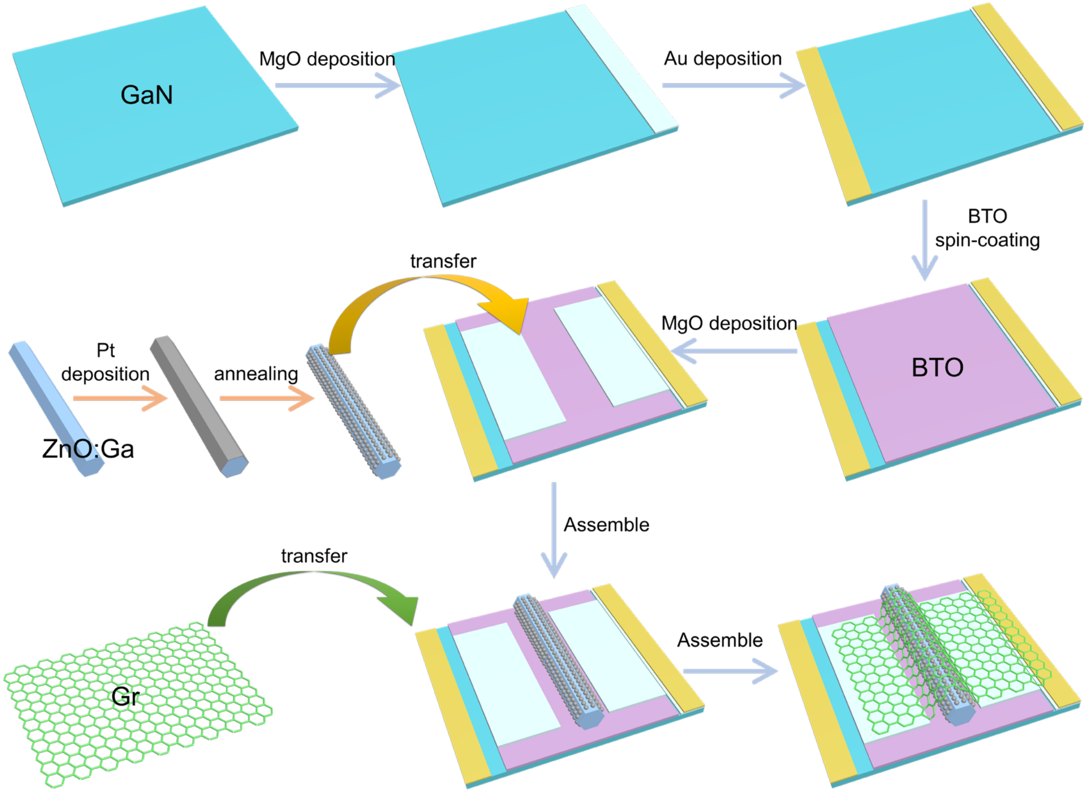

Figure S8. Schematic diagram of the fabrication flow of the PtNPs@ZnO:Ga/$BaTiO_3$/GaN heterojunction PD.

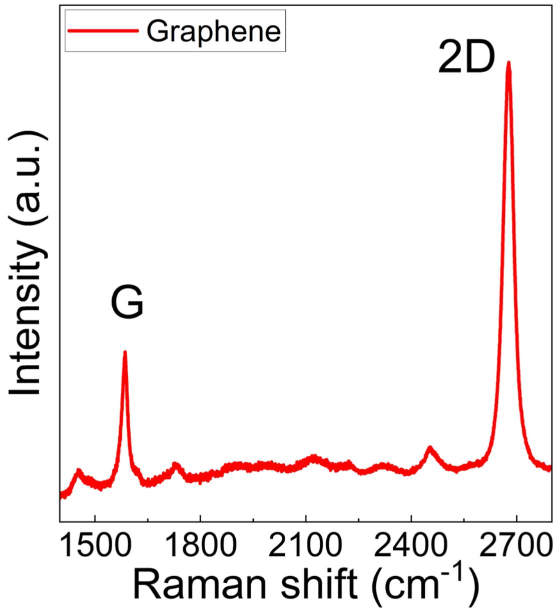

Figure S9. Room-temperature Raman spectra of the single-layer graphene.

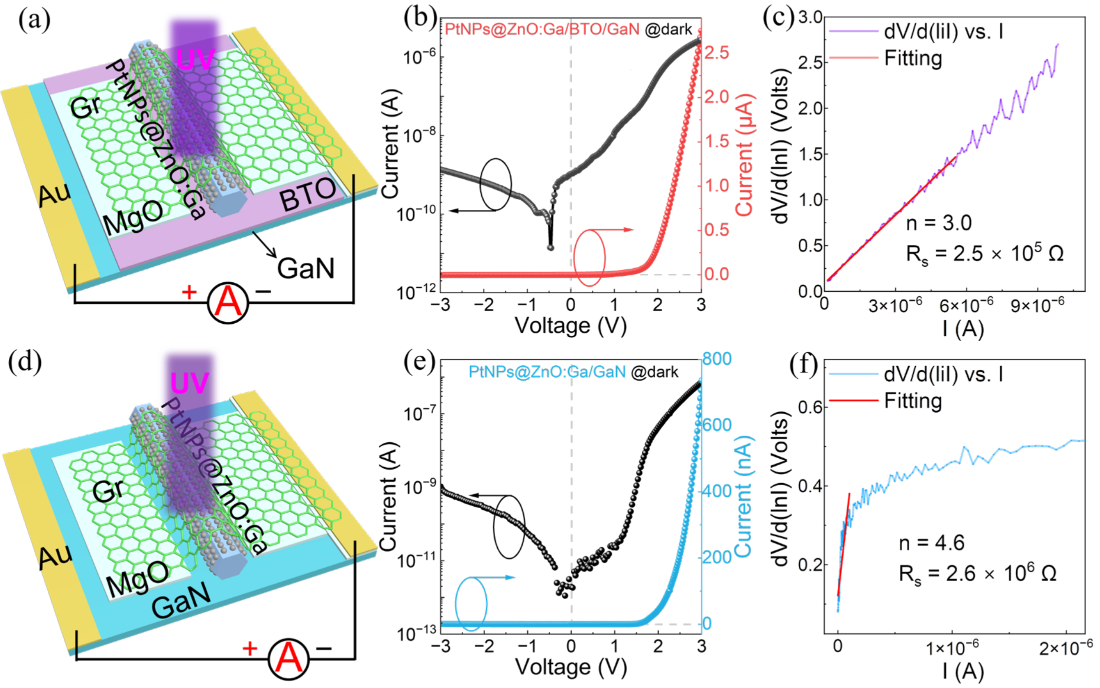

Figure S10. The calculation of the ideality factor and series resistance of the PtNPs@ZnO:Ga/BTO/GaN PD and PtNPs@ZnO:Ga/GaN PD. (a) Schematic architecture, (b) *I-V* curves plotted in the dark, and (c) Experimental d*V*/d(ln*I*) vs. *I* plot of the PtNPs@ZnO:Ga/BTO/GaN PD. (d) Schematic architecture, (e) *I-V* curves plotted in the dark, and (f) Experimental d*V*/d(ln*I*) vs. *I* plot of the PtNPs@ZnO:Ga/GaN PD.

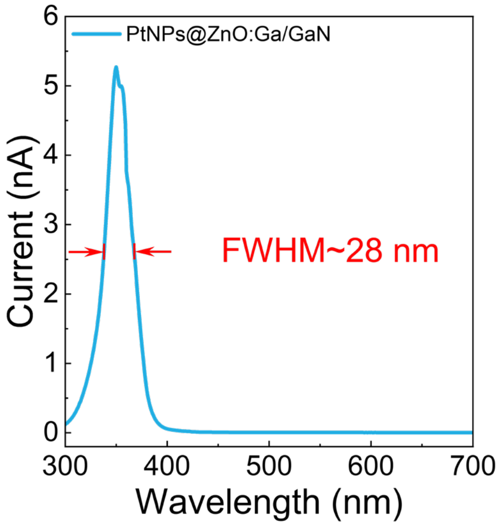

Figure S11. Light wavelength-dependent photocurrent of the PtNPs@ZnO:Ga/GaN PD.

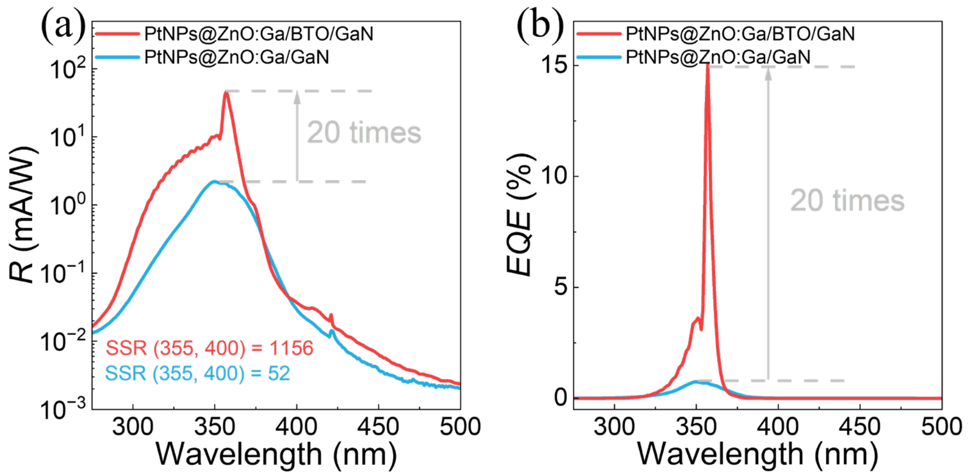

Figure S12. Photoresponse comparison of the PtNPs@ZnO:Ga/GaN heterojunctrion photodetectors, in which the devices were interfaced without and with BaTiO$_3$ nanolayer. Light wavelength-dependent (a) responsivities and (b) *EQE*s of the fabricated detectors.

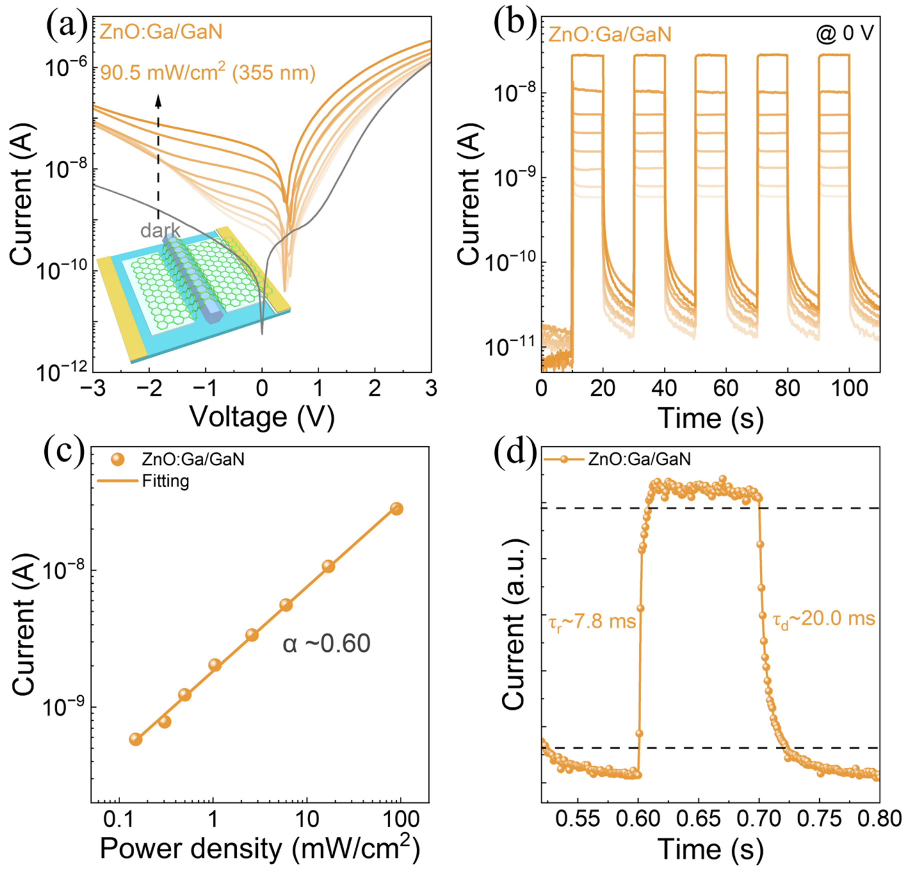

Figure S13. Photodetection performance of the ZnO:Ga/GaN heterojunction detector. (a) Logarithmic *I-V* characteristic curves, and (b) *I-t* curves of the ZnO:Ga/GaN PD under 355 nm irradiation with various light intensities. (c) Light power densitydependent current of the ZnO:Ga/GaN PD. (d) Single-cycle time-dependent photoresponse characteristics under 355 nm light illumination at 0 V bias.

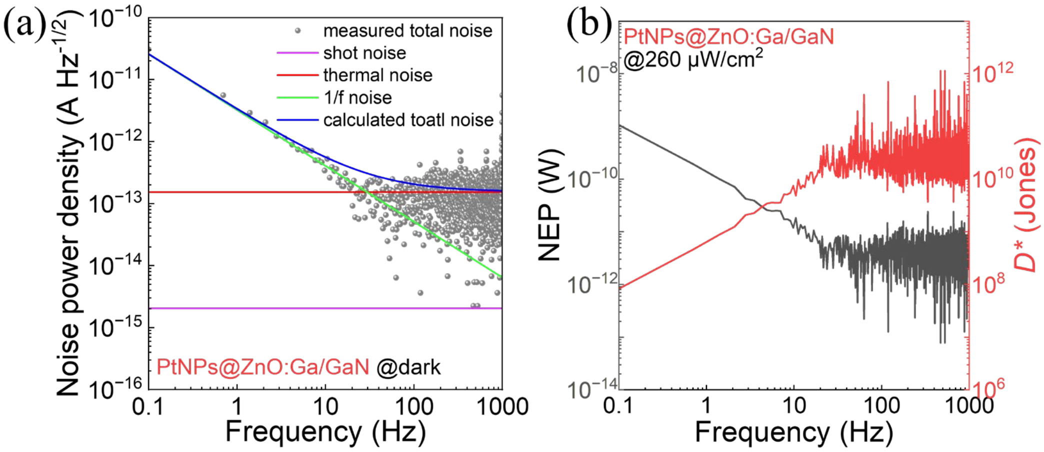

Figure S14. (a) Total noise power density spectrum obtained by Fourier transform of the time-domain dark current of the PtNPs@ZnO:Ga/GaN PD. (b) *NEP* and *D** of the device when tested in a self-biasing manner.

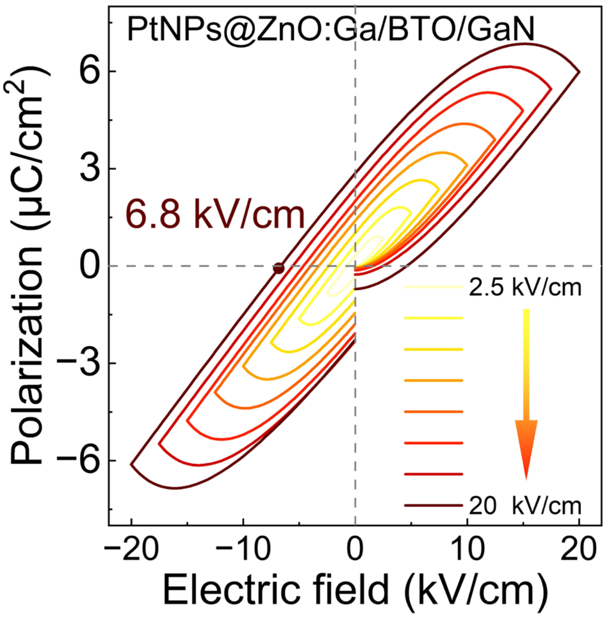

Figure S15. Electric field-dependent hysteresis loops of the PtNPs@ZnO:Ga/BaTiO$_3$/GaN heterojunction device.

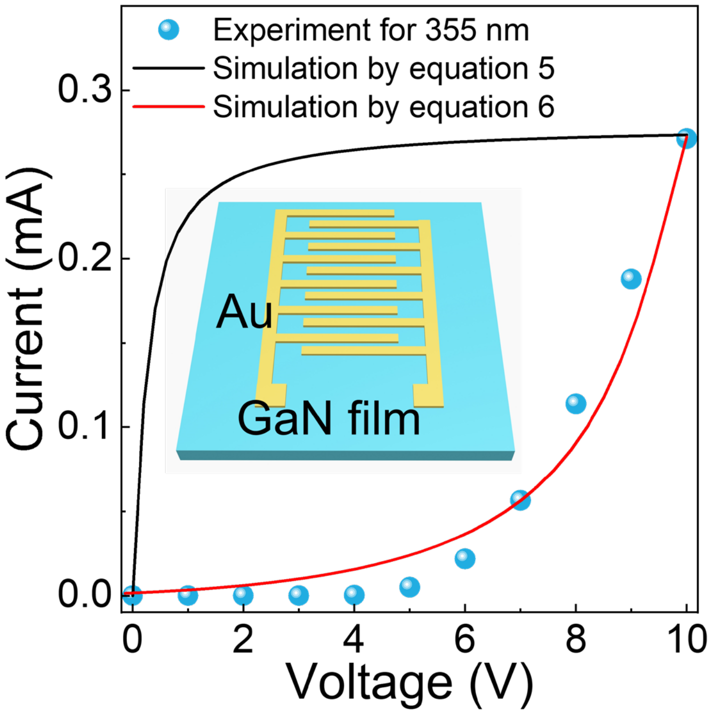

Figure S16. Electrical voltage-dependent photocurrent of the GaN film illuminated under 355 nm, and the calculated photocurrent using the Hecht equation and modified Hecht equation considering the exciton ionization.

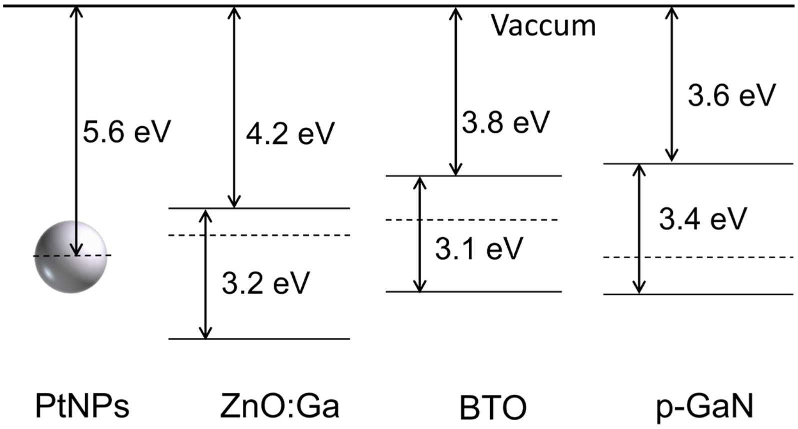

Figure S17. Schematic diagram of the energy band arrangement of PtNPs, ZnO:Ga, BTO, and GaN before contact.

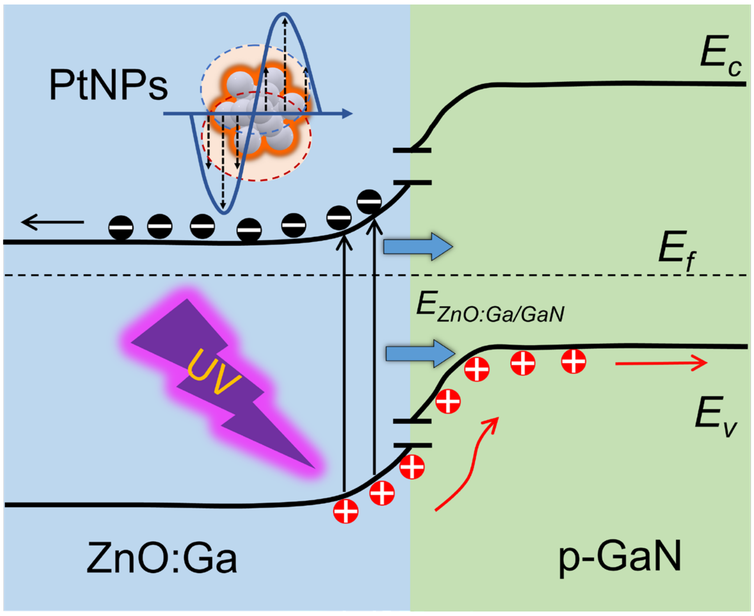

Figure S18. (a) The energy band diagram of PtNPs@ZnO:Ga/GaN heterojunction under UV light at zero bias.

1. Theoretical distribution width of depletion regions.[2]

The theoretical distribution width of depletion in p-GaN region (w_{GaN}) and in n-ZnO:Ga region ($w_{ZnO:Ga}$) can be evaluated through the formula:

$$w_{ZnO:Ga} = \sqrt{\frac{2\varepsilon_{ZnO:Ga}\varepsilon_0 n_{GaN} V_{in}}{e n_{ZnO:Ga}\left(n_{ZnO:Ga} + n_{GaN}\right)}} \tag{1}$$

$$w_{GaN} = \sqrt{\frac{2\varepsilon_{GaN}\varepsilon_0 n_{ZnO:Ga} V_{in}}{e n_{GaN}\left(n_{ZnO:Ga} + n_{GaN}\right)}} \tag{2}$$

Where $\varepsilon_{ZnO:Ga}$ is relative dielectric constants of ZnO (~8), ε_{GaN} is relative dielectric constants of GaN (~8.9). n_{GaN} (~5.0×10^{19}) and $n_{ZnO:Ga}$ (~8.2×10^{17}) are carrier concentrations, respectively. V_{in} is the built-in voltage (~1.0 V), ε_0 is the permittivity of vacuum, and e is elementary charge. From (1) and (2), $w_{ZnO:Ga}$ is calculated as 32.6 nm, and w_{GaN} is calculated as 0.5 nm.

2. The calculation of the electrical transport properties of ZnO:Ga MWs both with

and without PtNPs coating.

Based on the experimental results of Fig. S6, the electrical parameters like mobility, charge carrier concentration and conductivity, can be estimated using the following equations:

$$g_{\mathrm{m}} = \frac{\mathrm{d}I_{\mathrm{ds}}}{\mathrm{d}V_{\mathrm{g}}} = \frac{2\pi\varepsilon_0\varepsilon_{\mathrm{SiO_2}}\mu V_{\mathrm{ds}}}{L cosh^{-1}(1+2h/d)} \tag{3}$$

$$\sigma = \frac{1}{\rho} = \frac{L}{RS_{\mathrm{ZnO}}} = nq\mu \tag{4}$$

where the V_{ds} is set to 1.0 V, the ε_0, $\varepsilon_{\mathrm{SiO_2}}$, h, and d represent the vacuum electrostatic constant, the relative dielectric constant of SiO_2 ($\varepsilon_{\mathrm{SiO_2}}$ ~3.9), the thickness of SiO_2 (h ~300 nm), and the diameter of a ZnO:Ga MW(d ~15 μm), respectively.

3. The simulation of GaN-based MSM structure's photocurrent using the Hecht equation and modified Hecht equation considering the exciton ionization.

The GaN-based MSM structure was constructed to demonstrate the existence of the field-enhanced exciton ionization process within the thin film, considering that the excitons did not ionize at room temperature because of the high E_B. The current of the GaN-based MSM structure versus voltage is plotted, along with the calculated current using the modified Hecht equation with considering the field-enhanced exciton ionization,[3]

$$I(V) = I_0 V \frac{\mu\tau}{d^2}\left(1 - \mathrm{e}^{-d^2/\mu\tau V}\right) \tag{5}$$

$$I(V) = I_0 \mathrm{e}^{-(E_{\mathrm{B}} - eEa_{\mathrm{B}})/k_{\mathrm{B}}T} V \frac{\mu\tau}{d^2}\left(1 - \mathrm{e}^{-d^2/\mu\tau V}\right) \tag{6}$$

where I_0 is the saturation current of device, which is the current under 10 V, V is the applied bias, μ is the carrier mobility, τ is the carrier bulk recombination lifetime, d is the interelectrode spacing, E_B is the bulk exciton binding energy, e is the elementary charge, E is the electric intensity, k_B is the Boltzmann constant, T is the temperature, and a_B is the Bohr radius. When considering the field-enhanced exciton ionization process, $I_0 e^{-(E_B - eEa_B)/k_B T}$ can be regarded as the saturating current increasing with the electric intensity.

4. The calculation of the ideality factor and series resistance of the heterojunction diodes.

The diode parameters are determined from the forward current-voltage (*I-V*) characteristics, which is usually described within the thermionic emission theory:[4, 5]

$$I = I_o \exp\left(\frac{qV}{nkT}\right) \tag{7}$$

where the saturation current I_0 is expressed as:

$$I_o = aA^{**}T^2 \exp\left(\frac{-q\phi_{Bo}}{kT}\right) \tag{8}$$

where q is the electron charge, V is the applied voltage, A^{**} is the effective Richardson constant, a is the effective diode area, T is the absolute temperature, k is the Boltzmann constant, n is the ideality factor of diode, and ϕ_{B0} is the zero bias barrier height. For values of V greater than nkT/q, the ideality factor n from Eq. (7) can be written as:[6]

$$n = \frac{q}{kT}\frac{\Delta V}{\Delta \ln I} \tag{9}$$

The effect of the series resistance is usually modelled with series combination of a diode and a resistor R_s. The voltage V_d across the diode can be expressed in terms of the total voltage drop V across the diode and the resistance R_s. Thus, the $V_d = V - IR_s$ and the Eq. (7) can be expressed as:

$$I = I_o \exp\left(\frac{q\left(V - IR_s\right)}{nkT}\right) \tag{10}$$

At low bias, the ideality factor n and the resistance R_s of a heterojunction is expressed as follows:

$$\frac{dV}{d(\ln I)} = IR_S - \frac{nkT}{q} \tag{11}$$

Thus, the slope and *y*-axis intercept of a plot of $dV/d\ln I$ versus I will give R_s and nkT/q, respectively. The relevant parameters of the heterojunction diodes are calculated and summarized in the **Table I** for comparison. By introducing BTO in the PtNPs@ZnO:Ga/GaN heterojunction diode, the ideality factor and series resistance of the PtNPs@ZnO:Ga/BTO/GaN heterojunction diode are smaller than that of the PtNPs@ZnO:Ga/GaN heterojunction diode. The deviation of the ideality factor for both heterojunction diodes may originate from the interface or surface recombination of electrons and holes.

Table I. The dark *I*-*V* characteristics of PtNPs@ZnO:Ga/GaN heterojunction diode and PtNPs@ZnO:Ga/BTO/GaN heterojunction diode.

	PtNPs@ZnO:Ga/GaN	PtNPs@ZnO:Ga/BTO/GaN
Rectification ratio at ±3 V	7.0×10^{2}	2.0×10^{3}
Ideality factor (n)	4.6	3.0
Series resistance (Ω)	2.6×10^{6}	2.5×10^{5}

Reference

1. Y. Zhang, X. Y. Zhao, J. X. Chen, S. Y. Li, W. Yang and X. S. Fang, *Adv. Funct. Mater.*, 2020, **30**, 1907650.
2. P. Wan, M. Jiang, T. Xu, Y. Liu, X. Fang and C. Kan, *Adv. Opt. Mater.*, 2021, **10**, 2101851.
3. A. Mohite, J.-T. Lin, G. Sumanasekera and B. W. Alphenaar, *Nano Lett.*, 2006, **6**, 1369-1373.
4. S. K. Cheung and N. W. Cheung, *Appl. Phys. Lett.*, 1986, **49**, 85-87.
5. A. Keffous, M. Siad, S. Mamma, Y. Belkacem, C. Lakhdar Chaouch, H. Menari, A. Dahmani and W. Chergui, *Appl. Surf. Sci.*, 2003, **218**, 337-343.
6. L. Zeng, D. Wu, J. Jie, X. Ren, X. Hu, S. P. Lau, Y. Chai and Y. H. Tsang, *Adv. Mater.*, 2020, **32**, e2004412.